Engineering of Perovskite Materials Based on Formamidinium and Cesium Hybridization for High-Efficiency Solar Cells

Daniel Prochowicz,*,[†,‡] Rashmi Runjhun,[‡] Mohammad Mahdi Tavakoli,[†,§] Pankaj Yadav,[∥]
Marcin Saski,[‡] Anwar Q. Alanazi,[†] Dominik J. Kubicki,[†,⊥] Zbigniew Kaszkur,[‡] Shaik M. Zakeeruddin,[†]
Janusz Lewiński,*,[‡,#] and Michael Grätzel*,[†]

[†]Laboratory of Photonics and Interfaces, Institute of Chemical Sciences and Engineering, School of Basic Sciences and [⊥]Laboratory of Magnetic Resonance, Institute of Chemical Sciences and Engineering, Ecole Polytechnique Fédérale de Lausanne (EPFL), Lausanne CH-1015, Switzerland
[‡]Institute of Physical Chemistry, Polish Academy of Sciences, Kasprzaka 44/52, Warsaw 01-224, Poland
[§]Department of Materials Science and Engineering, Sharif University of Technology, Tehran 14588, Iran
[∥]Department of Solar Energy, School of Technology, Pandit Deendayal Petroleum University, Gandhinagar 382 007, Gujarat, India
[#]Faculty of Chemistry, Warsaw University of Technology, Noakowskiego 3, Warsaw 00-664, Poland

S *Supporting Information*

ABSTRACT: Engineering the chemical composition of inorganic−organic hybrid perovskite materials is an effective strategy to boost the performance and operational stability of perovskite solar cells (PSCs). Among the diverse family of ABX_3 perovskites, methylammonium-free mixed A-site cation $Cs_xFA_{1−x}PbI_3$ perovskites appear as attractive light-absorber materials because of their optimum band gap, superior optoelectronic property, and good thermal stability. Here, we develop a simple and very effective one-step solution method for the preparation of high-quality $(Cs)_x(FA)_{1−x}PbI_3$ perovskite films upon the addition of excess CsCl to the $FAPbI_3$ precursor solution. It is found that the addition of CsCl as a source of Cs cation instead of relevant addition of CsI to the parent perovskite solution increases effectively the grain size and film quality leading to improved charge mobility, reduced carrier recombination, and long carrier lifetime. The resultant mesoscopic perovskite devices exhibit a maximum efficiency of 20.60% with a stabilized power conversion efficiency of 19.85% and lower hysteresis compared to the reference device. This performance is among the highest reported for PSC devices incorporating mixed cation $(Cs)_x(FA)_{1−x}PbI_3$ perovskites.
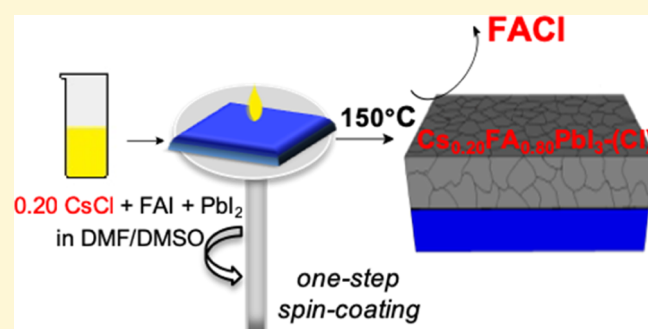
1. INTRODUCTION

Hybrid organic−inorganic metal halide perovskites have sparked the interest of the scientific community as promising light absorbers for next-generation photovoltaic devices because of their rapidly increasing power conversion efficiencies (PCEs) exceeding 23%, ease of fabrication, and low-cost processing.[1,2] The exceptional performance of perovskite solar cells (PSCs) is ascribed to outstanding material properties including sharp optical band edge, high absorption coefficient and charge mobility, low exciton binding energy, and long carrier diffusion lengths.[3−6] These perovskites share the chemical formula of ABX_3 (A = MA, FA, and Cs; B= Pb and Sn; and X = I, Br, and Cl), where the size of the three constituent ions follows the rule of Goldschmidt tolerance factor to sustain its cubic three-dimensional structure.[7,8] Compared to the extensively used methylammonium lead iodide,[9−11] formamidinium lead iodide ($FAPbI_3$) perovskite has attracted increasing research interests owing to its beneficial lower band gap red-shifted toward the single-

junction photovoltaic Shockley−Queisser optimum and improved thermal stability.[12,13] However, the photoactive $FAPbI_3$ phase (α-phase) is thermodynamically stable only above 150 °C and converts promptly to a yellow phase (δ-phase) at room temperature.[14−16] This phase transition is driven by the presence of relatively large FA cations that distort the perovskite lattice and can be suppressed by optimizing the Goldschmidt tolerance factor through the incorporation of smaller cations or halides leading to improved PCE and stability of devices.[17] Initial efforts to stabilize the α-phase perovskite focused on the introduction of an MA cation to $FAPbI_3$, which results in the formation of mixed-cation $(MA)_x(FA)_{1−x}PbI_3$ compositions.[18−21] However, these mixed-cation systems were found to exhibit limited thermal stability because of the volatile nature of the MA cation.[22] In

turn, the replacement of the A-site MA cation by a Cs cation, leading to a similar final $(Cs)_x(FA)_{1-x}PbI_3$ composition, has been reported to substantially improved phase stability against humidity and thermal stress compared with that of the parent $FAPbI_3$ perovskite.[23−25] For example, Lee et al. reported on the $Cs_{0.1}FA_{0.9}PbI_3$ composition showing enhanced thermal and moisture stability, reaching a PCE of 16.5%.[26] The improved structural stability was further explained by Yi et al. who showed that Cs is effective in assisting the crystallization of the α-phase in $FAPbI_3$ with up to 20% of Cs incorporation because of entropic stabilization.[27] The resulting mesoscopic solar cell employing the mixed-cation perovskite $Cs_{0.2}FA_{0.8}PbI_3$ yielded a maximum PCE of 15.69%.

The commonly used method to fabricate $(Cs)_x(FA)_{1-x}PbI_3$ perovskite films is the facile one-step spin-coating of a solution containing FAI, PbI_2, and CsI as a source of cesium cation in a certain stoichiometry.[26−28] Another way to fabricate $(Cs)_x(FA)_{1-x}PbI_3$ thin films is through a two-step deposition method, where a solution of PbI_2 and CsI is initially deposited onto the substrate, followed by sequential deposition of an FAI solution.[29,30] Recently, Zhou et al. developed a modified two-step processing approach by using a mixture of FAI and FACl in isopropanol during sequential deposition and achieved a PCE of 18.6%.[31] The usage of FACl was beneficial for the formation of the micrometer grain size film which facilitates the carrier transportation and collection.[31,32] Although mixed A-site cation $(Cs)_x(FA)_{1-x}PbI_3$-based PSCs exhibit excellent phase and thermal stability, their PCEs have not exceed 20%. Thus, further fabrication methods and device engineering need to be developed to boost the performance of this important perovskite family.

Herein, we report on a simple and effective one-step solution method for the preparation of a high-quality mixed A-site cation $(Cs)_x(FA)_{1-x}PbI_3$ perovskite active layer upon the addition of excessive amounts of CsCl to the equimolar mixture of FAI and PbI_2. This approach leads to intercalation of the Cs cation into the $FAPbI_3$ perovskite lattice, while the excessive chlorine anion sublimed as FACl at elevated temperature. This newly developed procedure increases effectively the grain size and film quality, leading to improved charge mobility, reduced nonradiative charge carrier recombination at grain boundaries (because of the presence of a lower density of defects and recombination centers in the perovskite film), and longer carrier lifetime. As a result, the mesoscopic heterojunction photovoltaic solar cell yields in a high PCE of 20.60% (stabilized at 19.85%) with low hysteresis effect.

2. RESULTS AND DISCUSSION

In this study, we employed the mixed-cation formulation of $(Cs)_{0.20}(FA)_{0.80}PbI_3$, previously optimized by Grätzel and co-workers,[27] as a reference perovskite-absorber layer. This composition was fabricated by spin-coating a solution containing PbI_2, FAI, and CsI with the molar ratio of 1:0.8:0.2 and followed by thermal annealing at 150 °C for 30 min (Scheme 1a). Our new one-step solution-processing approach for the formation of $(Cs)_{0.20}(FA)_{0.80}PbI_3$ perovskite films using CsCl as a source of cesium is schematically illustrated in Scheme 1b. We spin-coat the precursor solution comprising PbI_2, FAI, and CsCl with the molar ratio of 1:1:0.2 on the top of the TiO_2 film, followed by a similar annealing process as indicated above (for more details of perovskite film formation, see the Experimental Section). The mole fraction of CsCl in the equimolar mixture of PbI_2 and FAI was adjusted to

Scheme 1. Schematic Representation of the One-Step Spin-Coating Deposition Process of (a) $(Cs)_{0.20}(FA)_{0.80}PbI_3$ and (b) $(Cs)_{0.20}(FA)_{0.80}PbI_3$-(Cl) Films
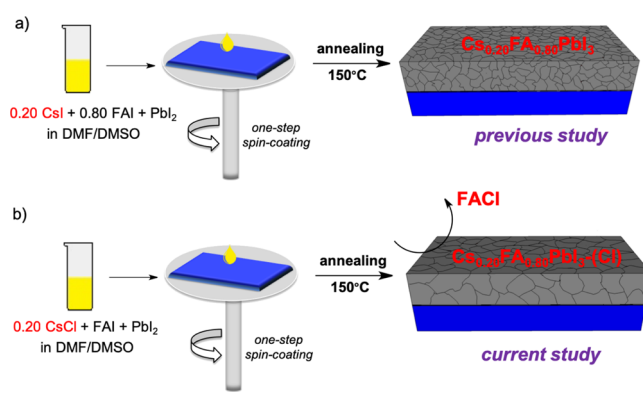
20% in order to achieve the final $(Cs)_{0.20}(FA)_{0.80}PbI_3$ composition after annealing and removal of the excessive amount of the FA cation. In this case, the thermal annealing leads to sublimation of FACl and the chloride anion introduced by CsCl facilitates removal of the excess amount of the FA cation at elevated temperature. The developed procedure improves the crystallinity of the perovskite film forming larger grains and reducing the recombination centers (vide infra).[33−36]

For simplicity, hereafter, we refer to the perovskite samples prepared using CsI and CsCl as $(Cs)_{0.20}(FA)_{0.80}PbI_3$-(I) and $(Cs)_{0.20}(FA)_{0.80}PbI_3$-(Cl), respectively. The dynamic light scattering (DLS) measurements on the both perovskite solutions reveal the presence of a similar size distribution of colloids (Figure S1). In order to confirm that the films prepared using the above two methods have the same composition, we carried out powder X-ray diffraction (PXRD) measurements and optical characterizations on the films. The PXRD patterns of $(Cs)_{0.20}(FA)_{0.80}PbI_3$-(I) and $(Cs)_{0.20}(FA)_{0.80}PbI_3$-(Cl) annealed at 150 °C are shown in Figure 1a. Although both samples display similar crystal structures with (001), (002), and (012) diffraction peaks centered at 14.07°, 28.3°, and 31.7°, the intensity of diffraction peaks becomes much stronger for the $(Cs)_{0.20}(FA)_{0.80}PbI_3$-(Cl) film compared with that of the reference film, indicating improved crystallinity upon CsCl addition. The absence of the characteristic peak near 12° in the PXRD pattern suggests a complete phase transformation from the δ-phase to the black α-phase. The peak located at 12.7° corresponds to the hexagonal phase of PbI_2 that can be associated with the decomposition of a small amount of perovskite at a high annealing temperature up to 150 °C.[37] Figure 1b shows the UV−vis absorption spectra of both the films, indicating a similar absorption spectrum over the entire visible region, which is in good agreement with the previous report.[27] In addition, the absorbance of $(Cs)_{0.20}(FA)_{0.80}PbI_3$-(Cl) is slightly higher than the reference perovskite film, supporting that the developed perovskite material can harvest more light, which should be favorable to enhance the solar cell performance. The estimated band gap from the UV−vis result shows a similar value of ∼1.56 eV for both materials. The steady-state photoluminescence (PL) spectra possess a similar PL peak position at 804 nm for both samples and the PL intensity increases significantly in $(Cs)_{0.20}(FA)_{0.80}PbI_3$-(Cl) as compared to the reference sample (Figure 1c). It is also consistent
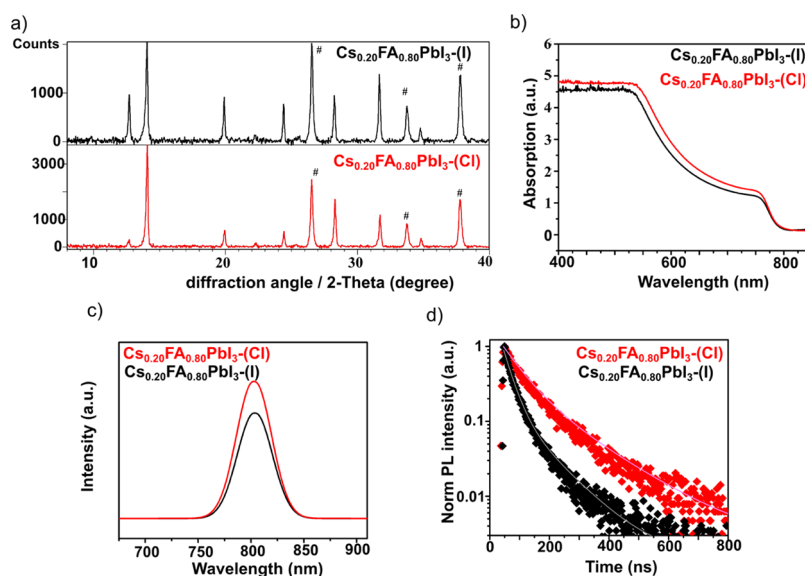
Figure 1. Characterization of the $(Cs)_{0.20}(FA)_{0.80}PbI_3$-(I) (black curve)- and $(Cs)_{0.20}(FA)_{0.80}PbI_3$-(Cl) (red curve)-processed perovskite films. (a) PXRD patterns [peaks marked with # corresponds to fluorine-doped tin oxide (FTO)]; (b) UV–vis absorption spectra; (c) steady-state PL spectra; and (d) time-resolved PL.

with the time-resolved PL (TRPL) result, where the $(Cs)_{0.20}(FA)_{0.80}PbI_3$-(Cl) film showed a much slower PL decay with carrier lifetime of 108.4 ns, in comparison with a carrier lifetime of 38.6 ns in the reference film (Figure 1d). The increased PL intensity found in the $(Cs)_{0.20}(FA)_{0.80}PbI_3$-(Cl) film indicates a decrease in nonradiative recombination originating from defects and trap states. Ultraviolet photoelectron spectroscopy (UPS) was employed to investigate in more detail the energy levels of $(Cs)_{0.20}(FA)_{0.80}PbI_3$-(I) and $(Cs)_{0.20}(FA)_{0.80}PbI_3$-(Cl). Figure S2 shows the UPS spectra of the two films, indicating that their Fermi levels lie at 4.62 and 4.89 eV for $(Cs)_{0.20}(FA)_{0.80}PbI_3$-(I) and $(Cs)_{0.20}(FA)_{0.80}PbI_3$-(Cl), respectively. The deeper Fermi level in $(Cs)_{0.20}(FA)_{0.80}PbI_3$-(Cl) suggests that the extent of band-bending at the perovskite/spiro-OMeTAD interface could be modified by the addition of CsCl. The estimated value of the valence band (5.39 eV) in the $(Cs)_{0.20}(FA)_{0.80}PbI_3$-(Cl) film is deeper than in the $(Cs)_{0.20}(FA)_{0.80}PbI_3$-(I) sample (5.37 eV). This small gap can be attributed to the slightly different amount of the FA cation in these perovskite compositions. As evidenced by PXRD, the reference sample has increased the intensity of the PbI_2 peak compared to the $(Cs)_{0.20}(FA)_{0.80}PbI_3$-(Cl) film, suggesting a higher degree of the perovskite degradation (Figure 1a). Moreover, the X-ray photoelectron spectroscopy (XPS) analysis shows the reduction of I/Pb molar ratio in the $(Cs)_{0.20}(FA)_{0.80}PbI_3$-(I) film compared to the $(Cs)_{0.20}(FA)_{0.80}PbI_3$-(Cl) film (see Figure S3 and Tables S1 and S2).

The morphological properties of the perovskite films were further analyzed by scanning electron microscopy (SEM) and atomic force microscopy (AFM) measurements. Plan view SEM images of both samples reveal pinhole-free films after annealing at 150 °C for 30 min (Figure 2a,b). The observed white spots on the both perovskite films indicate the appearance of traces of the PbI_2 phase, which well corroborated with the PXRD data. Notably, the $(Cs)_{0.20}(FA)_{0.80}PbI_3$-(Cl) film exhibits larger grain size (up to ~1 μm) than that of the reference film. Previous works demonstrated that the micrometer grain size film can be

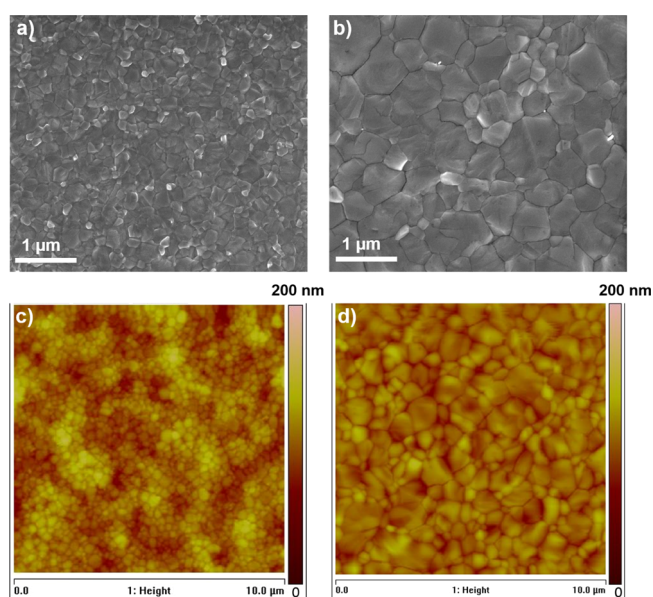**Figure 2.** Top view SEM and AFM images of perovskite films (a–c) $(Cs)_{0.20}(FA)_{0.80}PbI_3$-(I) and (b–d) $(Cs)_{0.20}(FA)_{0.80}PbI_3$-(Cl) deposited on FTO/compact TiO_2/mesoporous TiO_2.

obtained when FACl is employed together with FAI.[31,32] The AFM images of both perovskites are in good agreement with the SEM results (Figure 2c,d). Moreover, the root-mean-square surface roughness of perovskite films was estimated from AFM images to be 18 and 35 nm for $(Cs)_{0.20}(FA)_{0.80}PbI_3$-(Cl) and reference films, respectively, as shown in Figure S4. Previous reports demonstrated that the presence of chloride ions in the starting solution plays a key role in improving the growth of perovskite grain size and enhancing the photovoltaic performance of the resulting solar cells.[38,39] The signal of Cl atoms in the perovskite films treated with CsCl was not detected in the X-ray fluorescence (XRF) spectrum (Figure S5), indicating that the Cl atoms had been
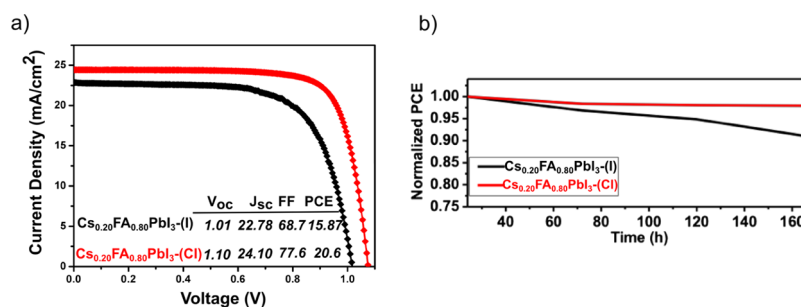
Figure 3. (a) $J-V$ scans for the best performing $(Cs)_{0.20}(FA)_{0.80}PbI_3$-(I) (black) and $(Cs)_{0.20}(FA)_{0.80}PbI_3$-(Cl) (red) PSCs and (b) shelf-life test of PSCs at room temperature stored inside a dry air box (30% RH) for the $(Cs)_{0.20}(FA)_{0.80}PbI_3$-(I) (black) and $(Cs)_{0.20}(FA)_{0.80}PbI_3$-(Cl) (red) devices.

removed during the annealing process because of the volatile nature of FACl.[32,33,40]

In order to demonstrate the occurrence of FACl sublimation, we conducted further studies on a free-standing powder (further referred to as $(Cs)_{0.20}(FA)_{0.80}PbI_3$-(Cl) (m)) obtained by grinding in a ball mill of the precursor salts CsCl/FAI/PbI_2 in a molar ratio of 0.2:1:1, respectively (for details, see the Experimental Section in the Supporting Information). Recently, we have demonstrated that the mechanochemical approach emerges as an appealing method for synthesizing large quantities of high-quality perovskites[21,41,42] and that the structure and composition of the resulting mechanoperovskites is indistinguishable on the molecular level from that of a thin film, as evidenced by solid-state NMR measurements.[43−45] Then, the as-grounded $(Cs)_{0.20}(FA)_{0.80}PbI_3$-(Cl) (m) powder was moved to vial, covered with a glass, and heated up to 150 °C for 30 min (Figure S6). The Fourier transform infrared (FTIR) spectrum of the evolved white substance confirms that FACl was sublimed from the perovskite powder during annealing at 150 °C (Figure S7). In addition, PXRD coupled with mass spectrometry measurement was carried out to identify the chemical composition of the released substance during the thermal annealing process of $(Cs)_{0.20}(FA)_{0.80}PbI_3$-(Cl) (m) powder. Figure S8 shows the mass-to-charge ratio (m/z) peaks recorded simultaneously during the thermal annealing of $(Cs)_{0.20}(FA)_{0.80}PbI_3$-(Cl) (m), which are identified as the fragmentation pattern of formamidine ions.

To test the effects of the morphological and carrier lifetime changes in $(Cs)_{0.20}(FA)_{0.80}PbI_3$-(Cl) films on the respective solar cell performance, we made devices of the architecture glass/FTO/bl-TiO_2/ms-TiO_2/perovskite/spiro-OMeTAD/Au (for details of the device fabrication, see the Experimental Section). The current−voltage ($J-V$) characteristics of champion $(Cs)_{0.20}(FA)_{0.80}PbI_3$-(I) and $(Cs)_{0.20}(FA)_{0.80}PbI_3$-(Cl) PSCs, measured under AM 1.5G irradiation at 100 mW cm^{-2}, are shown in Figure 3a. The $(Cs)_{0.20}(FA)_{0.80}PbI_3$-(I) device yields a PCE of 15.87% with a J_{sc} of 22.78 mA cm^{-2}, a V_{oc} of 1.01 V, and a fill factor (FF) of 68.7%. These photovoltaic parameters are close to those values previously obtained by Yi et al. in a similar device configuration.[27] In contrast, a superior photovoltaic performance is observed for $(Cs)_{0.20}(FA)_{0.80}PbI_3$-(Cl)-based PSC, which offers a significantly increased PCE of 20.60%, with a high V_{oc} of 1.10 V, a J_{sc} of 24.10 mA cm^{-2}, and an FF of 77.6%. The statistical distributions of the photovoltaic metrics are shown in Figure S9. Compared with the reference, $(Cs)_{0.20}(FA)_{0.80}PbI_3$-(Cl) PSCs show a higher average value of J_{sc} (~1.5 mA/cm^{-2}) and V_{oc} (~80 mV), thereby leading to an ~20% improvement in

average PCE. The integrated J_{sc} value calculated from the IPCE spectrum for $(Cs)_{0.20}(FA)_{0.80}PbI_3$-(Cl)-based device equals to 23.40 mA cm^{-2}, which agreed with the J_{sc} values obtained from the $J-V$ curves within an error of 3% showing a negligible spectral mismatch of our simulator with the standard AM 1.5 emission (Figure S10). The hysteresis indices (h) of the investigated devices were calculated from the formula $h = 100 \times (PCE_{RS} - PCE_{FS})/PCE_{RS}$, where PCE_{RS} and PCE_{FS} were the PCE from reverse and forward scans, respectively. As shown in Figure S11 and Table S3 (Supporting Information), the hysteresis indices of $(Cs)_{0.20}(FA)_{0.80}PbI_3$-(Cl) devices are lower than that of the reference cells. The lower hysteresis could be attributed to the larger grain size and uniform growth of the perovskite layer, which reduces the grain boundaries and improves the charge transfer between the grains.[46,47] To verify the high performance of the $(Cs)_{0.20}(FA)_{0.80}PbI_3$-(Cl)-based devices, stabilized power output was monitored over time (60 s) near the maximum power output point. Figure S12 shows the stabilized maximum power point tracking data of the best $(Cs)_{0.20}(FA)_{0.80}PbI_3$-(Cl) device with a steady-state efficiency of 19.85%, which is among the highest efficiencies reported on $Cs_xFA_{1-x}PbI_3$-based solar cells.[26,27,31,32] In addition, the shelf lifetime was also examined for the nonencapsulated cells by measuring the photovoltaic characteristic for 7 days. Figure 3b shows that the ambient stability of the $(Cs)_{0.20}(FA)_{0.80}PbI_3$-(Cl)-based device is greatly improved, which retains 98% of its initial PCE up to 160 h. On the contrary, the PCE of pristine $(Cs)_{0.20}(FA)_{0.80}PbI_3$-(I)-based device decays and reaches 90% of its initial efficiency.

The charge recombination in $(Cs)_{0.20}(FA)_{0.80}PbI_3$-(I) and $(Cs)_{0.20}(FA)_{0.80}PbI_3$-(Cl) devices was investigated by measuring light intensity dependence of V_{oc} and current−voltage scans under dark condition. Figure 4a shows the plot of V_{oc} versus the natural logarithm of light intensity for both the devices. The smaller slope of K_BT/q for the $(Cs)_{0.20}(FA)_{0.80}PbI_3$-(Cl) device suggests that the trap-assisted charge recombination process is suppressed as compared to the reference device. To further evaluate the charge recombination in the fabricated devices, the dark $J-V$ measurements were investigated using electrochemical impedance spectroscopy (EIS). Figure S13 illustrates the dark $J-V$ plot measured under forward scan for both the devices in logarithmic scale with respect to applied voltage. Ideality factor (n) of the fabricated devices was extracted by using the expression of $n(V) = (q/K_BT)J(V)(dJ/dV)^{-1}$, where q is the charge, K_B is the Boltzmann constant, and T is the cell temperature. The devices exhibit very similar values of n to those extracted from the V_{oc} versus illumination plots.
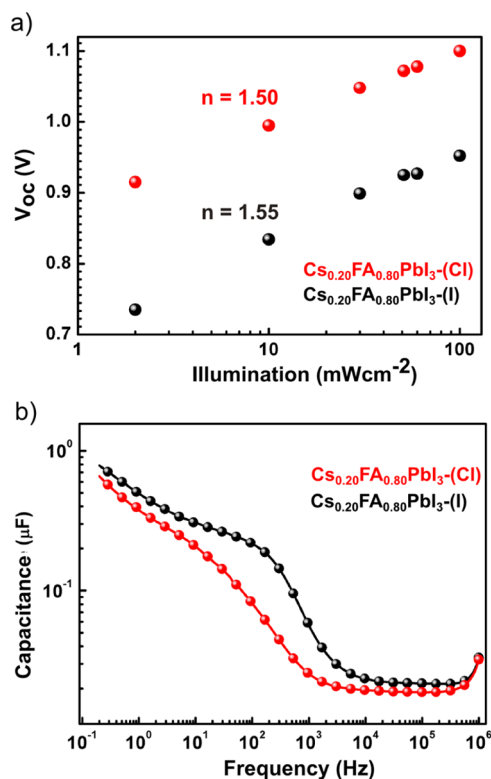
a)

b)

Figure 4. (a) Open-circuit voltage (V_{oc}) as a function of light intensity for $(Cs)_{0.20}(FA)_{0.80}PbI_3$-(I) and $(Cs)_{0.20}(FA)_{0.80}PbI_3$-(Cl) devices and (b) capacitance vs frequency spectra of $(Cs)_{0.20}(FA)_{0.80}PbI_3$-(I) and $(Cs)_{0.20}(FA)_{0.80}PbI_3$-(Cl) devices under dark at the short-circuit condition in the frequency range of 200 mHz to 1 MHz.

Moreover, a lower value of the net terminal or recombination current is observed for the $(Cs)_{0.20}(FA)_{0.80}PbI_3$-(Cl) device than that found in the reference device. To get further insights into the device recombination, EIS measurements under dark condition at different applied biases which represent two arc features corresponding to the low and high frequency were performed (Figure S14). Figure 4b shows the capacitance–frequency spectra for both the devices. The obtained EIS spectra were fitted by the electrical equivalent circuit shown in Figure S15. The physical interpretation of electrical equivalent circuit was discussed in our previous works.[48,49] Both devices show a comparable value of 12 Ω for series resistance (R_s). Figure S16 compares the extracted values of recombination resistance (R_{rec}) in these devices. The lower recombination current and higher value of R_{rec} in $(Cs)_{0.20}(FA)_{0.80}PbI_3$-(Cl) devices indicate a lower recombination. We note that our method allows to the fabrication of mesoscopic PSCs with lower hysteresis effect. This low value in $(Cs)_{0.20}(FA)_{0.80}PbI_3$-(Cl) devices can be correlated with the lower frequency capacitance (Figure 4b), while the higher value of low-frequency capacitance in reference devices was attributed to the accumulation of electronic and ionic charges at interfaces.[50] From the above results, we can attribute the lower recombination and charge accumulation in the $(Cs)_{0.20}(FA)_{0.80}PbI_3$-(Cl) PSCs to the improved surface morphology of the perovskite film.

3. CONCLUSIONS

In conclusion, a new effective synthetic protocol for the preparation of high-quality A-site mixed-cation $Cs_xFA_{1-x}PbI_3$ perovskite films was developed. The developed procedure allows for the preparation of high-quality $(Cs)_{0.20}(FA)_{0.80}PbI_3$ perovskite active layer upon the addition of excess CsCl to the $FAPbI_3$ precursor solution. We have shown that the resulted perovskite films possess a well-defined grain feature with improved crystallinity and larger grain size leading to longer carrier lifetime as compared to reference films. As a result, the mesoscopic heterojunction photovoltaic solar cell demonstrated an impressive PCE of 20.60% (stabilized at 19.85%) and low hysteresis effect. This method opens new opportunities toward mixed-cation $Cs_xFA_{1-x}PbI_3$ perovskite active layers with large grain size, high crystallinity, and outstanding photoelectricity conversion property, which can definitely lead to broader applications of hybrid perovskite materials.

4. EXPERIMENTAL SECTION

4.1. Materials. FAI was purchased from dyesol; PbI$_2$ was purchased from TCI, and CsI/CsCl salts were purchased from abcr GmbH. Titanium diisopropoxide bis(acetylacetonate) (75 wt % in isopropanol), lithium bis(trifluoro methanesulfonyl)imide (Li-TFSI), and 4-*tert*-butylpyridine were received from Sigma-Aldrich.

4.1.1. Solar Cell Device Fabrication. Nippon Sheet Glass 10 Ω/sq was selected for device fabrication. All substrates were cleaned by ultrasonic treatment in 2% Hellmanex water solution for 30 min and rinsed with deionized water and ethanol. Then, the substrates were cleaned by UV ozone for 15 min before fabrication. The compact TiO$_2$ layer was deposited by spray pyrolysis of 9 ml of ethanol solution containing 0.6 mL of titanium diisopropoxide bis-(acetylacetonate) solution (75% in 2-propanol, Sigma-Aldrich) and 0.4 mL of acetylacetone at 450 °C in air. Afterward, a thick mesoporous titanium dioxide layer was deposited on the TiO$_2$ electron transport layer by spin-coating 30 nm-sized nanoparticles (Dyesol 30NRD, Dyesol) diluted in ethanol (1:6 wt/wt) at 5000 rpm for 10 s. Then, the films were gradually heated to 500 °C and sintered at that temperature for 1.5 h under oxygen atmosphere. The reference perovskite solution in 1 mL of anhydrous dimethylformamide (DMF)/dimethyl sulfoxide (DMSO) (4:1; v/v) was prepared from PbI$_2$ (1 mmol; 0.461 g), FAI (0.80 mmol, 0.137 g), and CsI (0.2 mmol, 0.051 g) by vigorous stirring 60 °C for ≈12 h till the cloudy solution yields to a transparent yellow solution. The 1 M stock solution of $(Cs)_{0.20}(FA)_{0.80}PbI_3$(Cl) was prepared by dissolving PbI$_2$ (1 mmol; 0.461 g), FAI (1 mmol, 0.172 g), and CsCl (0.2 mmol, 0.033 g) in 1 ml of anhydrous DMF/DMSO (4:1; v/v) at 60 °C for ≈12 h till the cloudy solution yields to a transparent yellow solution. Thereafter, the perovskite solutions were spin-coated in two steps, that is, the perovskite solutions were deposited by spin-coating in a two-step program at 1000 rpm for 10 s and 6000 rpm for 20 s. In the second step, 100 μL of chlorobenzene (CB) was dropped on the top of the spinning film 10 s prior to the end of the program. After deposition, the film was annealed at 150 °C for 30 min in a dry box. Then, the hole transporting material solution was prepared by dissolving in 1 mL of CB 90 mg spiro-MeOTAD, 20.6 μL of lithium bis(trifluoromethylsulfonyl)imide (stock solution Li-TFSI 520 mg·mL^{-1} in acetonitrile), and 35.6 μL *tert*-butylpyridine and spin-coated at 4000 rpm for 20 s. Finally, gold as a thin top electrode (∼80 nm) was deposited by thermal evaporation under high vacuum.

4.1.2. Device Characterization. The photovoltaic curves were recorded using a Keithley (model 2400) digital source meter. The light source was a 450 W xenon lamp (Oriel) equipped with a Schott K113 Tempax sunlight filter (Praezisions Glas & Optik GmbH) to match the emission spectra to the AM1.5G standard in the region of 350−750 nm. The devices for *J*−*V* measurements were masked with a metal mask to give the active area of 0.16 cm^2. The potentiostat Biologic SP300 equipped with a frequency response analyzer was used

for ac measurements. EIS measurement was performed in the dc bias range of 0 to open-circuit voltage with an ac perturbation signal of 10 mV in the frequency range of 1 Hz to 100 kHz. The modulation current was set to be 10% of the dc background illumination intensity. The modulated cool white LED array (12 V, 10 W) light source was driven by a galvanostatic mode of Biologic SP-300. For shelf-life measurement, the devices were kept in a dry air box with a relative humidity of 30% and measured every 24 h under backward scan direction (10 mV as the step voltage) for 7 days.

4.2. Powder X-ray Diffraction. An X'Pert MPD PRO (PANalytical) diffractometer equipped with a ceramic tube (Cu anode, $\lambda = 1.54060$ A°), a secondary graphite (002) monochromator, and an RTMS X'Celerator (PANalytical) was used to record PXRD diffractograms. The samples were measured in an angle range of $2\theta = 5°$ to $40°$, by step scanning with a step of $0.02°$.

4.3. Powder X-ray Diffraction Coupled with Mass Spectrometry. A D5000 diffractometer (Bruker AXS) in Bragg–Brentano geometry using Cu Kα radiation (40 kV, 40 mA), a LynxEye strip detector, and a computer-controlled gas-feeding system coupled with a mass spectrometer (Hiden Analytical, HAL VII) were used for sample measurements. The sample (around 60 mg) was spread over a thin porous sintered glass disc and mounted vertically on the stainless steel heating block of our vacuum-proof XRD camera. The temperature was controlled via two RE-15 controllers (Lumel) and the K-type thermocouples. The measurements were performed under high-purity Ar (5.0) flown at 20 mL/min (mass flow controller MKS1259C).

4.4. Structure and Optical Characterization. The film morphology was studied by high-resolution SEM (Zeiss Merlin) and AFM (NanoScope IIIa/Dimension 3100). XRF spectra were acquired on an EDAX Orbis Vision (EDAX) XRF spectroscope using a beam energy of 30 keV. The energy resolution specified by the manufacturer is 0.132 keV. UV–vis measurements were recorded by a Varian Cary 5. TRPL spectra were carried out using a picosecond-pulsed diode laser (EPL-405, excitation wavelength 405 nm, pulse width 49 ps). For fitting, a biexponential equation was used and the lifetime was estimated from the following equation: $\tau_{avr} = t_1 t_2 / (t_1 + t_2)$. An ultraviolet photoelectron spectrometer (AXIS NOVA, Kratos Analytical Ltd, UK) was employed to record the valence and Fermi levels of perovskite films using He I (21.2 eV) as the photon source. FTIR attenuated total reflectance (FTIR–ATR) spectrum was recorded on a Bruker Tensor apparatus equipped with the ATR accessory. The colloid size distribution was determined by DLS performed on a Malvern Zetasizer Nano Z (Malvern Instruments, UK).

4.5. X-ray Photoelectron Spectroscopy. A PHI VersaProbe II scanning XPS microprobe (Physical Instruments AG, Germany) equipped with a monochromatic Al Kα X-ray source of 24.8 W power with a beam size of 100 μm was used for XPS measurements. The spherical capacitor analyzer was set at 45° take-off angle with respect to the sample surface. The pass energy was 46.95 eV yielding a full width at half-maximum of 0.91 eV for the Ag $3d_{5/2}$ peak. The PHI MultiPak software was used for curve fitting.

ASSOCIATED CONTENT

Ⓢ Supporting Information

The Supporting Information is available free of charge on the ACS Publications website at DOI: 10.1021/acs.chemmater.8b04871.

> DLS graphs; UPS graphs; XPS spectra; AFM images; XRF spectra; IR and mass spectrometry data; statistic histogram; IPCE spectra; current density versus voltage characteristics; stability test; EIS spectra under dark condition; and recombination resistance as a function of applied bias under dark (PDF)

AUTHOR INFORMATION

Corresponding Authors
*E-mail: dprochowicz@ichf.edu.pl (D.P.).
*E-mail: lewin@ch.pw.edu.pl (J.L.).
*E-mail: michael.graetzel@epfl.ch (M.G.).

ORCID Ⓞ
Daniel Prochowicz: 0000-0002-5003-5637
Mohammad Mahdi Tavakoli: 0000-0002-8393-6028
Dominik J. Kubicki: 0000-0002-9231-6779
Janusz Lewiński: 0000-0002-3407-0395
Michael Grätzel: 0000-0002-0068-0195

Notes
The authors declare no competing financial interest.

ACKNOWLEDGMENTS

REFERENCES

(1) Yang, W. S.; Park, B.-W.; Jung, E. H.; Jeon, N. J.; Kim, Y. C.; Lee, D. U.; Shin, S. S.; Seo, J.; Kim, E. K.; Noh, J. H.; et al. Iodide management in formamidinium-lead-halide-based perovskite layers for efficient solar cells. *Science* **2017**, *356*, 1376–1379.

(2) Jeon, N. J.; Na, H.; Jung, E. H.; Yang, T.-Y.; Lee, Y. G.; Kim, G.; Shin, H.-W.; Il Seok, S.; Lee, J.; Seo, J. A Fluorene-Terminated Hole-Transporting Material for Highly Efficient and Stable Perovskite Solar Cells. *Nat. Energy* **2018**, *3*, 682–689.

(3) Stranks, S. D.; Eperon, G. E.; Grancini, G.; Menelaou, C.; Alcocer, M. J. P.; Leijtens, T.; Herz, L. M.; Petrozza, A.; Snaith, H. J. Electron-Hole Diffusion Lengths Exceeding 1 Micrometer in an Organometal Trihalide Perovskite Absorber. *Science* **2013**, *342*, 341–344.

(4) Wehrenfennig, C.; Eperon, G. E.; Johnston, M. B.; Snaith, H. J.; Herz, L. M. High Charge Carrier Mobilities and Lifetimes in Organolead Trihalide Perovskites. *Adv. Mater.* **2013**, *26*, 1584–1589.

(5) Shi, D.; Adinolfi, V.; Comin, R.; Yuan, M.; Alarousu, E.; Buin, A.; Chen, Y.; Hoogland, S.; Rothenberger, A.; Katsiev, K.; et al. Low Trap-State Density and Long Carrier Diffusion in Organolead Trihalide Perovskite Single Crystals. *Science* **2015**, *347*, 519–522.

(6) Dong, Q.; Fang, Y.; Shao, Y.; Mulligan, P.; Qiu, J.; Cao, L.; Huang, J. Electron-Hole Diffusion Lengths > 175 m in Solution-Grown $CH_3NH_3PbI_3$ Single Crystals. *Science* **2015**, *347*, 967–970.

(7) Kieslich, G.; Sun, S.; Cheetham, A. K. Solid-state principles applied to organic-inorganic perovskites: new tricks for an old dog. *Chem. Sci.* **2014**, *5*, 4712–4715.

(8) Saparov, B.; Mitzi, D. B. Organic-Inorganic Perovskites: Structural Versatility for Functional Materials Design. *Chem. Rev.* **2016**, *116*, 4558–4596.

(9) Burschka, J.; Pellet, N.; Moon, S.-J.; Humphry-Baker, R.; Gao, P.; Nazeeruddin, M. K.; Grätzel, M. Sequential Deposition as a Route to High-Performance Perovskite-Sensitized Solar Cells. *Nature* **2013**, *499*, 316–319.

(10) Liu, M.; Johnston, M. B.; Snaith, H. J. Efficient Planar Heterojunction Perovskite Solar Cells by Vapour Deposition. *Nature* **2013**, *501*, 395−398.

(11) Son, D.-Y.; Lee, J.-W.; Choi, Y. J.; Jang, I.-H.; Lee, S.; Yoo, P. J.; Shin, H.; Ahn, N.; Choi, M.; Kim, D.; Park, N.-G. Self-Formed Grain Boundary Healing Layer for Highly Efficient CH3NH3PbI3 Perovskite Solar Cells. *Nat. Energy* **2016**, *1*, 16081.

(12) Yang, W. S.; Noh, J. H.; Jeon, N. J.; Kim, Y. C.; Ryu, S.; Seo, J.; Seok, S. I. High-Performance Photovoltaic Perovskite Layers Fabricated through Intramolecular Exchange. *Science* **2015**, *348*, 1234−1237.

(13) Mu, C.; Pan, J.; Feng, S.; Li, Q.; Xu, D. Quantitative Doping of Chlorine in Formamidinium Lead Trihalide (FAPbI$_{3−x}$Cl$_x$) for Planar Heterojunction Perovskite Solar Cells. *Adv. Energy Mater.* **2016**, *7*, 1601297.

(14) Stoumpos, C. C.; Malliakas, C. D.; Kanatzidis, M. G. Semiconducting Tin and Lead Iodide Perovskites with Organic Cations: Phase Transitions, High Mobilities, and Near-Infrared Photoluminescent Properties. *Inorg. Chem.* **2013**, *52*, 9019−9038.

(15) Eperon, G. E.; Stranks, S. D.; Menelaou, C.; Johnston, M. B.; Herz, L. M.; Snaith, H. J. Formamidinium Lead Trihalide: A Broadly Tunable Perovskite for Efficient Planar Heterojunction Solar Cells. *Energy Environ. Sci.* **2014**, *7*, 982.

(16) Jeon, N. J.; Noh, J. H.; Kim, Y. C.; Yang, W. S.; Ryu, S.; Seok, S. I. Solvent engineering for high-performance inorganic-organic hybrid perovskite solar cells. *Nat. Mater.* **2014**, *13*, 897−903.

(17) Ono, L. K.; Juarez-Perez, E. J.; Qi, Y. Progress on Perovskite Materials and Solar Cells with Mixed Cations and Halide Anions. *ACS Appl. Mater. Interfaces* **2017**, *9*, 30197−30246.

(18) Pellet, N.; Gao, P.; Gregori, G.; Yang, T.-Y.; Nazeeruddin, M. K.; Maier, J.; Grätzel, M. Mixed-Organic-Cation Perovskite Photovoltaics for Enhanced Solar-Light Harvesting. *Angew. Chem., Int. Ed.* **2014**, *53*, 3151−3157.

(19) Ji, F.; Wang, L.; Pang, S.; Gao, P.; Xu, H.; Xie, G.; Zhang, J.; Cui, G. A Balanced Cation Exchange Reaction toward Highly Uniform and Pure Phase FA$_{1−x}$MA$_x$PbI$_3$ Perovskite Films. *J. Mater. Chem. A* **2016**, *4*, 14437−14443.

(20) Yang, Z.; Chueh, C.-C.; Liang, P.-W.; Crump, M.; Lin, F.; Zhu, Z.; Jen, A. K.-Y. Effects of Formamidinium and Bromide Ion Substitution in Methylammonium Lead Triiodide toward High-Performance Perovskite Solar Cells. *Nano Energy* **2016**, *22*, 328−337.

(21) Prochowicz, D.; Yadav, P.; Saliba, M.; Saski, M.; Zakeeruddin, S. M.; Lewiński, J.; Grätzel, M. Mechanosynthesis of Pure Phase Mixed-Cation MA$_x$FA$_{1−x}$PbI$_3$ Hybrid Perovskites: Photovoltaic Performance and Electrochemical Properties. *Sustainable Energy Fuels* **2017**, *1*, 689−693.

(22) Binek, A.; Hanusch, F. C.; Docampo, P.; Bein, T. Stabilization of the Trigonal High-Temperature Phase of Formamidinium Lead Iodide. *J. Phys. Chem. Lett.* **2015**, *6*, 1249−1253.

(23) Li, Z.; Yang, M.; Park, J.-S.; Wei, S.-H.; Berry, J. J.; Zhu, K. Stabilizing Perovskite Structures by Tuning Tolerance Factor: Formation of Formamidinium and Cesium Lead Iodide Solid-State Alloys. *Chem. Mater.* **2015**, *28*, 284−292.

(24) Liu, T.; Zong, Y.; Zhou, Y.; Yang, M.; Li, Z.; Game, O. S.; Zhu, K.; Zhu, R.; Gong, Q.; Padture, N. P. High-Performance Formamidinium-Based Perovskite Solar Cells via Microstructure-Mediated δ-to-α Phase Transformation. *Chem. Mater.* **2017**, *29*, 3246−3250.

(25) Bella, F.; Renzi, P.; Cavallo, C.; Gerbaldi, C. Caesium for Perovskite Solar Cells: An Overview. *Chem.—Eur. J.* **2018**, *24*, 12183−12205.

(26) Lee, J.-W.; Kim, D.-H.; Kim, H.-S.; Seo, S.-W.; Cho, S. M.; Park, N.-G. Formamidinium and Cesium Hybridization for Photo- and Moisture-Stable Perovskite Solar Cell. *Adv. Energy Mater.* **2015**, *5*, 1501310.

(27) Yi, C.; Luo, J.; Meloni, S.; Boziki, A.; Ashari-Astani, N.; Grätzel, C.; Zakeeruddin, S. M.; Röthlisberger, U.; Grätzel, M. Entropic Stabilization of Mixed A-Cation ABX$_3$ Metal Halide Perovskites for

High Performance Perovskite Solar Cells. *Energy Environ. Sci.* **2016**, *9*, 656−662.

(28) Xu, X.; Ma, C.; Xie, Y.-M.; Cheng, Y.; Tian, Y.; Li, M.; Ma, Y.; Lee, C.-S.; Tsang, S.-W. Air-Processed Mixed-Cation Cs$_{0.15}$FA$_{0.85}$PbI$_3$ Planar Perovskite Solar Cells Derived from a PbI$_2$−CsI−FAI Intermediate Complex. *J. Mater. Chem. A* **2018**, *6*, 7731−7740.

(29) Xia, X.; Wu, W.; Li, H.; Zheng, B.; Xue, Y.; Xu, J.; Zhang, D.; Gao, C.; Liu, X. Spray Reaction Prepared FA$_{1−x}$Cs$_x$PbI$_3$ Solid Solution as a Light Harvester for Perovskite Solar Cells with Improved Humidity Stability. *RSC Adv.* **2016**, *6*, 14792−14798.

(30) Huang, J.; Xu, P.; Liu, J.; You, X.-Z. Sequential Introduction of Cations Deriving Large-Grain Cs$_x$FA$_{1−x}$PbI$_3$ Thin Film for Planar Hybrid Solar Cells: Insight into Phase-Segregation and Thermal-Healing Behavior. *Small* **2016**, *13*, 1603225.

(31) Zhou, N.; Shen, Y.; Zhang, Y.; Xu, Z.; Zheng, G.; Li, L.; Chen, Q.; Zhou, H. CsI Pre-Intercalation in the Inorganic Framework for Efficient and Stable FA$_{1−x}$Cs$_x$PbI$_3$(Cl) Perovskite Solar Cells. *Small* **2017**, *13*, 1700484.

(32) Chen, J.; Xu, J.; Zhao, C.; Zhang, B.; Liu, X.; Dai, S.; Yao, J. Efficient Planar Heterojunction FA$_{1−x}$Cs$_x$PbI$_3$ Perovskite Solar Cells with Suppressed Carrier Recombination and Enhanced Open Circuit Voltage via Anion-Exchange Process. *ACS Appl. Mater. Interfaces* **2019**, *11*, 4597−4606.

(33) Yu, H.; Wang, F.; Xie, F.; Li, W.; Chen, J.; Zhao, N. The Role of Chlorine in the Formation Process of "CH$_3$NH$_3$PbI$_{3-x}$Cl$_x$" Perovskite. *Adv. Funct. Mater.* **2014**, *24*, 7102−7108.

(34) Lv, S.; Pang, S.; Zhou, Y.; Padture, N. P.; Hu, H.; Wang, L.; Zhou, X.; Zhu, H.; Zhang, L.; Huang, C.; et al. One-Step, Solution-Processed Formamidinium Lead Trihalide (FAPbI$_{(3−x)}$Cl$_x$) for Mesoscopic Perovskite−Polymer Solar Cells. *Phys. Chem. Chem. Phys.* **2014**, *16*, 19206−19211.

(35) Eperon, G. E.; Bryant, D.; Troughton, J.; Stranks, S. D.; Johnston, M. B.; Watson, T.; Worsley, D. A.; Snaith, H. J. Efficient, Semitransparent Neutral-Colored Solar Cells Based on Microstructured Formamidinium Lead Trihalide Perovskite. *J. Phys. Chem. Lett.* **2014**, *6*, 129−138.

(36) Prochowicz, D.; Yadav, P.; Saliba, M.; Kubicki, D. J.; Tavakoli, M. M.; Zakeeruddin, S. M.; Lewiński, J.; Emsley, L.; Grätzel, M. One-Step Mechanochemical Incorporation of an Insoluble Cesium Additive for High Performance Planar Heterojunction Solar Cells. *Nano Energy* **2018**, *49*, 523−528.

(37) Pool, V. L.; Dou, B.; Van Campen, D. G.; Klein-Stockert, T. R.; Barnes, F. S.; Shaheen, S. E.; Ahmad, M. I.; van Hest, M. F. A. M.; Toney, M. F. Thermal Engineering of FAPbI$_3$ Perovskite Material via Radiative Thermal Annealing and in Situ XRD. *Nat. Commun.* **2017**, *8*, 14075.

(38) Liang, P.-W.; Chueh, C.-C.; Xin, X.-K.; Zuo, F.; Williams, S. T.; Liao, C.-Y.; Jen, A. K.-Y. High-Performance Planar-Heterojunction Solar Cells Based on Ternary Halide Large-Band-Gap Perovskites. *Adv. Energy Mater.* **2014**, *5*, 1400960.

(39) Fan, L.; Ding, Y.; Luo, J.; Shi, B.; Yao, X.; Wei, C.; Zhang, D.; Wang, G.; Sheng, Y.; Chen, Y.; et al. Elucidating the Role of Chlorine in Perovskite Solar Cells. *J. Mater. Chem. A* **2017**, *5*, 7423−7432.

(40) Wang, Z.; Zhou, Y.; Pang, S.; Xiao, Z.; Zhang, J.; Chai, W.; Xu, H.; Liu, Z.; Padture, N. P.; Cui, G. Additive-Modulated Evolution of HC(NH$_2$)$_2$PbI$_3$ Black Polymorph for Mesoscopic Perovskite Solar Cells. *Chem. Mater.* **2015**, *27*, 7149−7155.

(41) Prochowicz, D.; Franckevičius, M.; Cieślak, A. M.; Zakeeruddin, S. M.; Grätzel, M.; Lewiński, J. Mechanosynthesis of the Hybrid Perovskite CH$_3$NH$_3$PbI$_3$: Characterization and the Corresponding Solar Cell Efficiency. *J. Mater. Chem. A* **2015**, *3*, 20772−20777.

(42) Prochowicz, D.; Yadav, P.; Saliba, M.; Saski, M.; Zakeeruddin, S. M.; Lewiński, J.; Grätzel, M. Reduction in the Interfacial Trap Density of Mechanochemically Synthesized MAPbI$_3$. *ACS Appl. Mater. Interfaces* **2017**, *9*, 28418−28425.

(43) Kubicki, D. J.; Prochowicz, D.; Hofstetter, A.; Zakeeruddin, S. M.; Grätzel, M.; Emsley, L. Phase Segregation in Cs-, Rb- and K-

Doped Mixed-Cation $(MA)_x(FA)_{1-x}PbI_3$ Hybrid Perovskites from Solid-State NMR. *J. Am. Chem. Soc.* **2017**, *139*, 14173−14180.

(44) Kubicki, D. J.; Prochowicz, D.; Hofstetter, A.; Saski, M.; Yadav, P.; Bi, D.; Pellet, N.; Lewiński, J.; Zakeeruddin, S. M.; Grätzel, M.; Emsley, L. Formation of Stable Mixed Guanidinium-Methylammonium Phases with Exceptionally Long Carrier Lifetimes for High-Efficiency Lead Iodide-Based Perovskite Photovoltaics. *J. Am. Chem. Soc.* **2018**, *140*, 3345−3351.

(45) Kubicki, D. J.; Prochowicz, D.; Hofstetter, A.; Zakeeruddin, S. M.; Grätzel, M.; Emsley, L. Phase Segregation in Potassium-Doped Lead Halide Perovskites from ^{39}K Solid-State NMR at 21.1 T. *J. Am. Chem. Soc.* **2018**, *140*, 7232−7238.

(46) Nie, W.; Tsai, H.; Asadpour, R.; Blancon, J.-C.; Neukirch, A. J.; Gupta, G.; Crochet, J. J.; Chhowalla, M.; Tretiak, S.; Alam, M. A.; et al. High-Efficiency Solution-Processed Perovskite Solar Cells with Millimeter-Scale Grains. *Science* **2015**, *347*, 522−525.

(47) Gedamu, D.; Asuo, I. M.; Benetti, D.; Basti, M.; Ka, I.; Cloutier, S. G.; Rosei, F.; Nechache, R. Solvent-Antisolvent Ambient Processed Large Grain Size Perovskite Thin Films for High-Performance Solar Cells. *Sci. Rep.* **2018**, *8*, 12885.

(48) Yadav, P.; Prochowicz, D.; Saliba, M.; Boix, P.; Zakeeruddin, S.; Grätzel, M. Interfacial Kinetics of Efficient Perovskite Solar Cells. *Crystals* **2017**, *7*, 252.

(49) Yadav, P.; Turren-Cruz, S.-H.; Prochowicz, D.; Tavakoli, M. M.; Pandey, K.; Zakeeruddin, S. M.; Grätzel, M.; Hagfeldt, A.; Saliba, M. Elucidation of Charge Recombination and Accumulation Mechanism in Mixed Perovskite Solar Cells. *J. Phys. Chem. C* **2018**, *122*, 15149−15154.

(50) Ngo, T. T.; Barea, E. M.; Tena-Zaera, R.; Mora-Seró, I. Spray-Pyrolyzed ZnO as Electron Selective Contact for Long-Term Stable Planar $CH_3NH_3PbI_3$ Perovskite Solar Cells. *ACS Appl. Energy Mater.* **2018**, *1*, 4057−4064.